



 Cite this: *RSC Adv.*, 2021, 11, 15486

First-principles predictions of low lattice thermal conductivity and high thermoelectric performance of AZnSb (A = Rb, Cs)†

 Enamul Haque 

Here, two compounds, AZnSb (A = Rb, Cs), have been predicted to be potential materials for thermoelectric device applications at high temperatures by using first-principles calculations based on density functional theory (DFT), density functional perturbation theory (DFPT), and Boltzmann transport theory. The layered structure, and presence of heavier elements Rb/Cs and Sb induce high anharmonicity (larger values of mode Grüneisen parameter), low Debye temperature, and intense phonon scattering. Thus, these compounds possess intrinsically low lattice thermal conductivity (κ_l), $\sim 0.5 \text{ W m}^{-1} \text{ K}^{-1}$ on average at 900 K. Highly non-parabolic bands and relatively wide bandgap (~ 1.37 and 1.1 eV for RbZnSb and CsZnSb, respectively, by mBJ potential including spin-orbit coupling effect) induce large Seebeck coefficient while highly dispersive and two-fold degenerate bands induce high electrical conductivity. Large power factor and low values of κ_l lead to a high average thermoelectric figure of merit (ZT) of RbZnSb and CsZnSb, reaching 1.22 and 1.1 and 0.87 and 1.14 at 900 K for p- and n-type carriers, respectively.

Received 11th March 2021

Accepted 21st April 2021

DOI: 10.1039/d1ra01938d

rsc.li/rsc-advances

1. Introduction

Many ABX compounds with 111 stoichiometry form either ZrBeSi or PbFCl type structures.^{1–3} These compounds have been found or predicted to exhibit some useful properties for practical applications, such as topological electronic structure.^{1–3} That's why topological materials have gained huge research interest to explore their potential applications in advanced electronic devices and their physical properties.^{4–9} Some of the antimony-based compounds exhibit topological behavior and its combination with other elements can crystallize in a wide range of structures, from zero to 3-dimensional motifs.^{9–15} These structures can be either too simple or too complex. The Sb-based compounds have thus a wide range of applications as thermoelectrics, photovoltaic, and other electronic components. A complex structured semi-conducting material usually possesses low lattice thermal conductivity due to intense phonon scattering and exhibits practically useful thermoelectric performance. Yb₁₄MnSb₁₁, a complex structured p-type material, is a well-known material for thermoelectric device applications at high temperatures.^{16,17}

In recent decades, the demand for clean energy increases day by day and researchers are searching for novel materials with high thermoelectric performance. The thermoelectric performance of a material depends on its Seebeck coefficient (S), electrical conductivity (σ), total thermal conductivity ($\kappa_{\text{tot}} = \kappa_e + \kappa_l$, electronic (κ_e) plus lattice thermal

conductivity (κ_l)), and absolute temperature (T). Many compounds have been found to exhibit large thermoelectric performance at high temperatures^{18,19} while others exhibit at low temperatures.^{20,21} The thermoelectric performance is defined by the expression²²

$$ZT = \frac{S^2 \sigma}{\kappa_{\text{tot}}} T$$

From the above expression, the high-performance thermoelectric materials are required to possess a large Seebeck coefficient, high electrical conductivity, and low total thermal conductivity. A high-temperature thermoelectric material must have an optimum electronic bandgap to avoid carrier excitons at high temperatures. The lattice thermal conductivity is also a crucial factor for a large ZT value, which may be reduced through nano-structuring^{23,24} and alloying with suitable dopant.^{25,26} The search for a suitable dopant is very critical because it requires an extensive study through large computational resources or experimental setup. Therefore, the materials with intrinsic low lattice thermal conductivity and high electrical conductivity will enhance the thermoelectric device performance significantly.

Some 111 ABX hypothetical compounds were predicted by Zhang *et al.* in 2012.²⁷ In this study, the authors reported the energetic stability of these compounds from first-principles study that the compounds are favorable to form in the laboratory.²⁷ They predicted that RbZnSb is formable in the LiYSn-type structure,²⁷ a disordered ZrBeSi-type structure. In the last year, Owens-Baird *et al.* successfully synthesized AZnSb (A = Rb, Cs) compounds,² which crystallize in the ZrBeSi-type structure. They reported that the melting or decomposition temperature of RbZnSb and CsZnSb is 975 and 1040 K, respectively.²

EH Solid State Physics Laboratory, Longaer, Gaffargaon-2233, Mymensingh, Bangladesh. E-mail: enamul.phy15@yahoo.com

† Electronic supplementary information (ESI) available. See DOI: 10.1039/d1ra01938d



From first-principles based electronic structure calculations by using PBE functional, Owens-Baird *et al.* also reported that the AZnSb compounds are topologically trivial narrow bandgap semiconductors.² The PBE functional underestimates the bandgap severely.²⁸ To date, the accurate electronic structure and thermoelectric properties of these layered AZnSb compounds have not been reported. Besides, Gorai *et al.* predicted from first-principles calculations that KSnBi, RbSnBi, and NaGeP exhibit good thermoelectric performance for n-type carriers, and these compounds are n-type dopable.²⁹ Therefore, it is worth studying the thermoelectric properties of AZnSb. In this article, I have reported the details of lattice dynamics, electronic structure by mBJ potential including spin-orbit coupling effect, and carrier transport properties of AZnSb. The AZnSb exhibit highly anisotropic transport properties and low lattice thermal conductivity, leading to a high average ZT of RbZnSb and CsZnSb, to 1.22 and 1.1 and 0.87 and 1.14 at 900 K for p- and n-type carriers, respectively.

2. Computational details

By using experimental values of the lattice parameters and atomic coordinates, the structural relaxations were performed in Quantum Espresso (QE) code³⁰ with the PBEsol³¹ setting of generalized gradient approximation (GGA).³² In the QE,³⁰ 42 Ry cutoff energy for wavefunctions, $12 \times 12 \times 6$ k -point, energy threshold 10^{-10} Ry, force convergence threshold 10^{-5} Ry/Au, and projector-augmented wave (PAW) pseudopotentials (from PSLibrary 1.0 (ref. 33)) were set in these calculations after extensive trials. The phonon dispersions and density of states were also calculated by using the same setting in QE. Then EPA code based on energy bins³⁴ was used to calculate average electron-phonon dynamical matrix. The sensitivity to the energy bins of EPA method was verified by using EPA-MLS code.³⁵ The resulted dynamical matrix was fed into BoltzTraP,³⁶ a code implementing the Boltzmann transport equation (BTE) using constant relaxation time approximation (CRTA). To calculate the carrier lifetime, the BoltzTraP code was modified slightly to read the dynamical matrix. As the BoltzTraP requires energy eigenvalues, the electronic structure calculations were performed in Wien2K,^{37,38} a full-potential linearized augmented plane wave method (FP-LAPW) based code. In these calculations, PBEsol functional with mBJ potential including spin-orbit coupling effect (SOC) was used for accurate bandgap. Besides, A, Zn, and Sb sphere radii (R_{mt}) 2.3, 2.21, 2.21 bohr, valence band and conduction band separation energy -7.0 Ry, and kinetic energy cutoff $R_{\text{mt}}K_{\text{max}} = 7.0$, a finer k -mesh $53 \times 53 \times 17$, energy convergence 1×10^{-6} Ry and charge convergence $0.001e$ were set in Wien2K during these calculations. The values of cutoff energy, k -point, *etc.* were selected after extensive trials, in such a way that the increase of these parameters does not change the total energy more than 1 meV.

By using the finite displacement method in Phono3py,³⁹ the lattice thermal conductivity and other auxiliary parameters were calculated by creating 221 supercells. The second and third-order interatomic force constants (IFCs) were calculated in QE by using the same setting as before except the k -point ($2 \times 2 \times 2$ in this case). The resulted IFCs were fed into Phono3py to solve the phonon Boltzmann transport

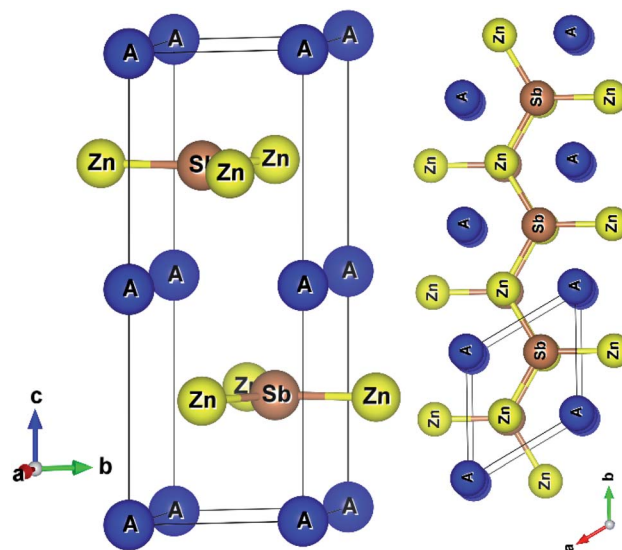


Fig. 1 Layered crystal structures of AZnSb, (a) unit cell of AZnSb, and (b) side view of AZnSb.

equation (pBTE) within the CRTA by using $14 \times 14 \times 14$ q -point. This approach to calculating lattice thermal conductivity has been found to predict the lattice thermal conductivity reliably.^{40–42}

3. Results and discussion

AZnSb compounds form a layered hexagonal structure with space group $P6_3/mmc$ (#194),² as shown in Fig. 1. The structures are well-known AlB_2 -type and three non-equivalent atoms have three unique positions in the unit cell.

Graphene like layers of Zn_3Sb_3 stacking along cross-plane (z -axis) are formed, where two Zn_3Sb_3 rings from adjoining layers create a hexagonal prism locating the alkali metal at the center of the prism. The computed hexagonal lattice parameters are listed in Table 1. As usual, the PBEsol functional underestimates the experimental lattice parameters by less than one percent.

Table 1 Computed lattice parameters, elastic constants (C_{ij}), bulk modulus (B), shear modulus (G), longitudinal sound velocity (v_l), transverse sound velocity (v_t), and Debye temperature⁴³ along with available experimental data

Parameters	RbZnSb		CsZnSb	
	Computed	Exp. ²	Computed	Exp. ²
a (Å)	4.5144	4.5466	4.5297	4.5588
c (Å)	11.0629	11.0999	11.8698	11.9246
c_{11} (GPa)	80.7	—	70.7	—
c_{12} (GPa)	24.5	—	21.9	—
c_{13} (GPa)	7.70	—	7.73	—
c_{33} (GPa)	33.8	—	39.3	—
c_{44} (GPa)	11.8	—	11.9	—
B (GPa)	27.4	—	26.7	—
G (GPa)	18.8	—	18.0	—
v_t (km s ⁻¹)	2.024	—	1.897	—
v_l (km s ⁻¹)	3.380	—	3.184	—
θ_D (km s ⁻¹)	208.3	—	190.4	—

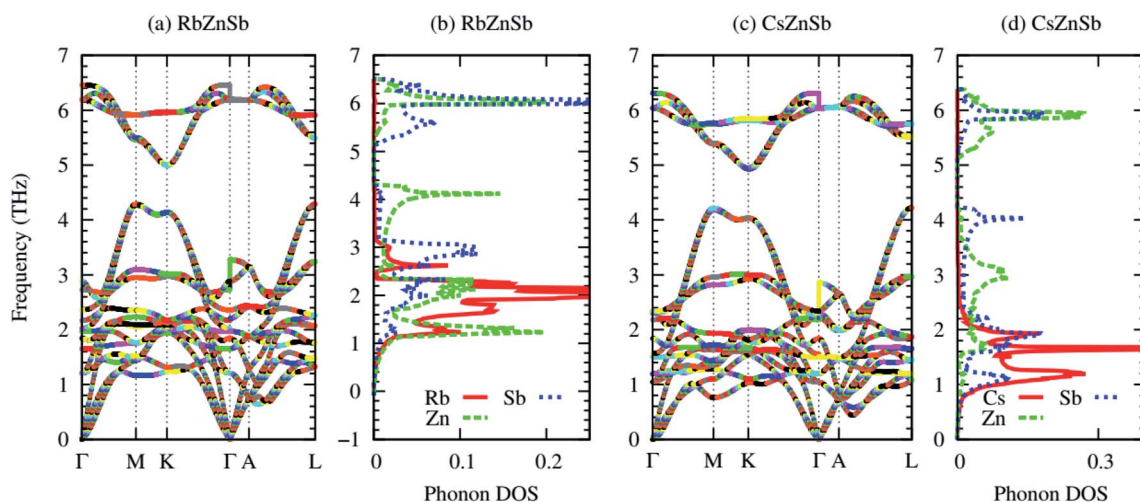


Fig. 2 Phonon dispersion and atom projected density of states of RbZnSb (a–b) and CsZnSb (c–d), respectively. In the phonon dispersion, longitudinal and transverse optical (LO–TO) phonon splittings have been included by calculating macroscopic dielectric constant and Born effective charge (listed in the ESI†).

The in-plane length (a) of AZnSb is almost independent of Rb/Cs's radii. As the Rb/Cs atoms are located between Zn–Sb layers, the cross-plane (c) length of the unit cell depends on their atomic radii. The elastic constants (listed in Table 1) of AZnSb satisfy the mechanical stability criteria described in ref. 44. The small value of the bulk modulus suggests that both compounds are less resistive to the external mechanical forces. According to Slack expression, the lattice thermal conductivity is directly proportional to the cube of the Debye temperature. In both compounds, the longitudinal and transverse sound propagates slowly, leading to a low value of the Debye temperature. The computed values of the Debye temperature of AZnSb are comparable to that of Bi_2Te_3 , which possesses intrinsically low lattice thermal conductivity.²¹

3.1. Lattice dynamics

Fig. 2 demonstrates the dynamical stability of AZnSb compounds, as the phonon dispersions contain no negative frequencies over the Brillouin zone (BZ). The acoustic and lower

energy optical phonons of RbZnSb arise from alkali metal (A) and Zn, while higher energy optical phonons are induced from Zn and Sb.

However, the acoustic and lower energy optical phonons of CsZnSb originate from Cs and Sb with small contributions from Zn. The acoustic and lower energy optical phonons have usually major contributions in the heat conduction. From the phonon dispersion, it is clear that the acoustic and optical phonons are overlapped largely, which are non-conductive for heat. Metal antimonide (Sb) has a dominant contribution to the lower energy phonon, as shown in the atom projected phonon density of states in Fig. 2(b and d).

The cross-plane phonons induced from covalently-bonded Zn–Sb may have a negligible contribution to the lattice thermal conductivity.

One of the most important phonon scattering factors, namely the Grüneisen parameter, has been calculated from second and third IFCs and presented graphically in Fig. 3. Unlike few ABX half-Heusler compounds, such as NbCoSb ⁴⁵ and ZrCoSb ,⁴⁶ with positive Grüneisen parameters values only, the mode Grüneisen parameter (γ) of AZnSb expands over positive and negative values for both

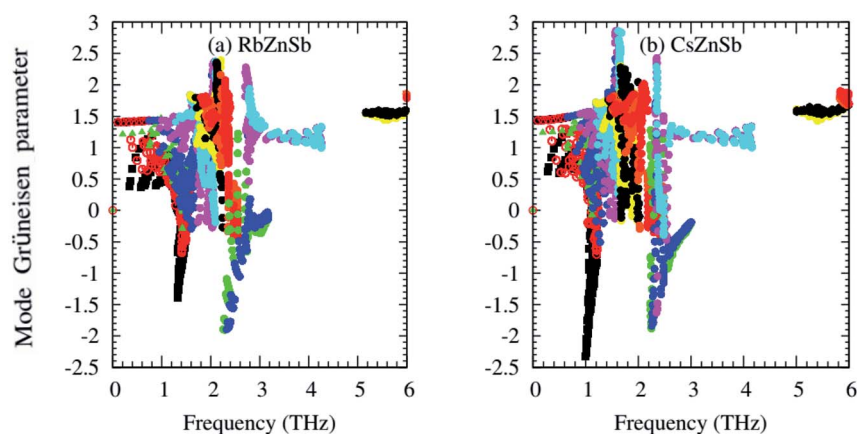


Fig. 3 Computed mode Grüneisen parameter from second and third-order IFCs.

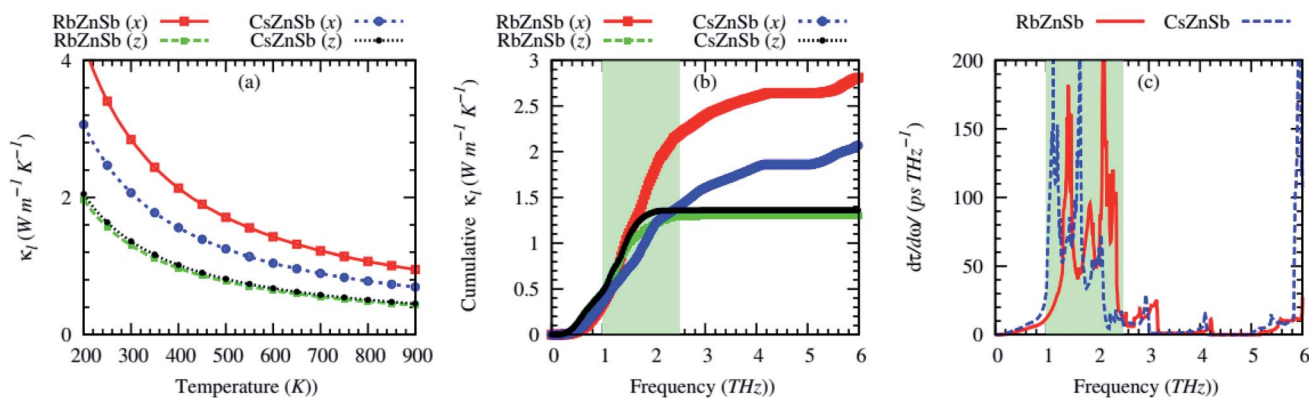


Fig. 4 Computed in-plane (x) and cross-plane (z) lattice thermal conductivity as a function of temperature (a), cumulative lattice thermal conductivity at 300 K as a function of phonon frequency (b), and (c) first-derivative of cumulative phonon lifetime, the shaded regions indicates the dominant acoustic-optical phonons scattering.

compounds. The presence of heavier elements Rb/Cs may be responsible for the negative values of the mode Grüneisen parameter of AZnSb. That's why the negative values of γ of CsZnSb are larger than that of RbZnSb. The negative values of the γ suggest that the external effect, such as pressure/temperature, may easily cause the contraction of the compounds and these compounds would have negative values of the thermal expansion coefficient.⁴⁷

Larger values of γ indicate high anharmonicity and *vice versa*. Both compounds possess larger values of γ , and thus, AZnSb compounds are highly anharmonic crystals due to their complex structure and heavier elements Rb/Cs and Sb-induced phonon softening. Therefore, such intense phonon scattering may lead to low lattice thermal conductivity. Let's have a look at it.

Fig. 4 shows the calculated anisotropic lattice thermal conductivity (κ_l) as a function of temperature. The κ_l values of both compounds are highly anisotropic due to the structural anisotropy. Both compounds possess relatively low lattice thermal conductivity (on average, $\kappa_l < 2$ W m⁻¹ K⁻¹ at 300 K) due to high

anharmonicity. Such low values of κ_l of both compounds are relatively higher than that of few typical thermoelectric materials possessing ultralow values of κ_l , for example, Cs₂PtI₆ (0.15 W m⁻¹ K⁻¹, Tl₃VSe₄ (0.30 W m⁻¹ K⁻¹ at 300 K (ref. 48)), Tl₂O (0.17 W m⁻¹ K⁻¹ at 300 K (ref. 49)), and SnSe (κ_l (along *b*-axis) = 0.7 W m⁻¹ K⁻¹ at 300 K (ref. 50)), at 300 K (ref. 51)), but comparable to that of NbCoSb (~2.5 W m⁻¹ K⁻¹ (the sample synthesized at 900 °C) at 300 K (ref. 52)) and in-plane κ_l of best low-temperature thermoelectric Bi₂Te₃ (1.6 W m⁻¹ K⁻¹ at 300 K (ref. 48)). However, the room temperature κ_l values are much smaller than that of typical ABX thermoelectrics HfCoSb (~14 W m⁻¹ K⁻¹ at 400 K (ref. 53) and ZrCoSb (~15 W m⁻¹ K⁻¹ at 300 K (ref. 54)).

Interestingly, the cross-plane κ_l of AZnSb is almost independent of alkali metal (Rb/Cs), although the cross-plane (*c*) length of the unit cell strongly depends on Rb/Cs. Generally, the κ_l exhibits opposite trend to the structural anisotropy, *i.e.*, the shorter the length of the unit cell along a certain direction will cause higher κ_l in that direction compared to other directions.

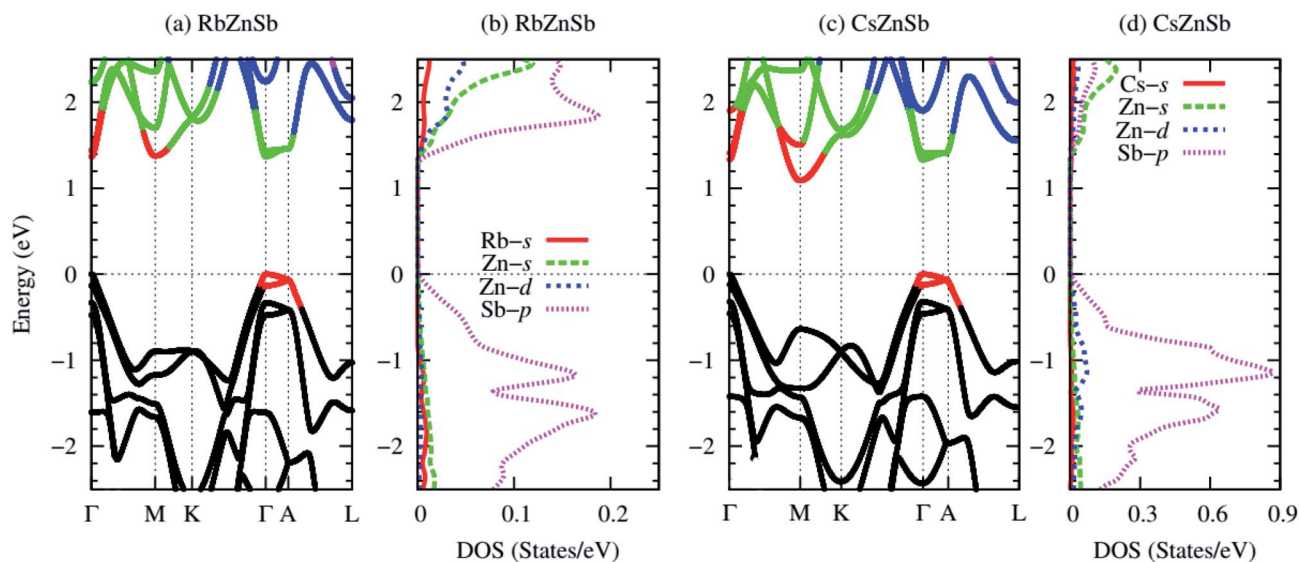


Fig. 5 Electronic bandstructure along with high symmetry points and projected density of states of RbZnSb (a–b) and CsZnSb (c–d), respectively. The dashed horizontal lines at zero energy represent the Fermi level.

Table 2 Computed electronic bandgap and effective mass by using mBJ potential including SOC effect

Parameters	RbZnSb	CsZnSb
E_g (eV)	1.37	1.1
Hole effective mass ($m_h^*(m_0)$)	1.23	1.13
Electron effective mass ($m_e^*(m_0)$)	0.14	0.15

From Fig. 4(b), the majority of heat is conducted by acoustic and optical phonons with energy ~ 1 –2.5 THz. Higher energy optical phonons have almost negligible contributions to the heat conduction. The first derivative of cumulative phonon lifetime indicates that acoustic and optical phonons (induced from Rb/Cs–Sb) with energy ~ 1 –2.5 THz have the strongest interactions, as shown by the shadow region in Fig. 4(c).

3.2. Electronic structure

Electronic structure analysis is crucial for characterizing a thermoelectric material. Fig. 5 demonstrates the computed band structures and projected density of states of AZnSb by using PBEsol functional with mBJ potential including the SOC effect. Both compounds exhibit almost identical band structures. The conduction and valence bands are highly dispersive bands. The strong interaction between Zn-4s and Sb-5p states dominantly induces the dispersive nature of electronic bands. The topmost valence bands and lowest conduction bands of both compounds are two-fold degenerate bands with three valleys, *i.e.*, the band degeneracy is six ($N_v = 6$). These degenerate bands originate from the structural symmetries, *i.e.*, the presence of rotational and one inversion symmetry. The shape of the computed bandstructures shows an excellent agreement with that reported in ref. 2 by using PBE functional including SOC effect.

Table 2 lists the computed bandgap and effective mass of AZnSb. Both compounds are direct bandgap semiconductors. The computed values of the bandgap are much higher than those reported (0.3 eV) in ref. 2 by using PBE functional. The

PBE functional cannot fully compensate the unphysical self-interaction energy which pushes the occupied states upward, and thus, severely underestimates the bandgap.²⁸ For example, the bandgap of ZnO calculated by PBE functional is 0.82 eV, while the experimental value is 3.44 eV and mBJ gives 2.71 eV.²⁸

Fig. 5(b and d) demonstrates the orbital projected density of states of both compounds. The conduction bands near the Fermi level mainly arise from Zn-4s and Sb-5p states. The valence bands near the Fermi level originate mainly from Zn-3d and Sb-5p states. However, the alkali metal Rb/Cs has a negligible contribution in bandgap formulation. The slight reduction of the bandgap of CsZnSb compared to the RbZnSb is due to the change of unit cell length along the z-axis. As Rb/Cs has a significant contribution to the lattice thermal conductivity and negligible contributions to the electronic structure, doping with a suitable element on this cation site may be an effective way to optimize the thermoelectric performance further. The valence band maxima (VBM) and conduction band minima (CBM) are highly non-parabolic bands, which will favor a larger Seebeck coefficient, while the degenerate and dispersive band will be favorable for high electrical conductivity.

3.3. Carrier transport

The original BoltzTraP code calculates the transport coefficients within cRTA.³⁶ To estimate the electrical conductivity and electronic part of the thermal conductivity, the code is required to modify for the calculation of carrier lifetime (relaxation time).

In the modified code, the carrier lifetime (τ) is calculated by the following equation³⁴

$$\tau^{-1}(\varepsilon, \mu, T) = \frac{2\pi\Omega}{g_s\hbar} \sum_v \left\{ g_v^2(\varepsilon, \varepsilon + \bar{\omega}_v) \left[n(\bar{\omega}_v, T) + f(\varepsilon + \bar{\omega}_v, \mu, T) \right] \rho(\varepsilon + \bar{\omega}_v) + g_v^2(\varepsilon, \varepsilon - \bar{\omega}_v) \left[n(\bar{\omega}_v, T) + 1 - f(\varepsilon - \bar{\omega}_v, \mu, T) \right] \rho(\varepsilon - \bar{\omega}_v) \right\} \quad (1)$$

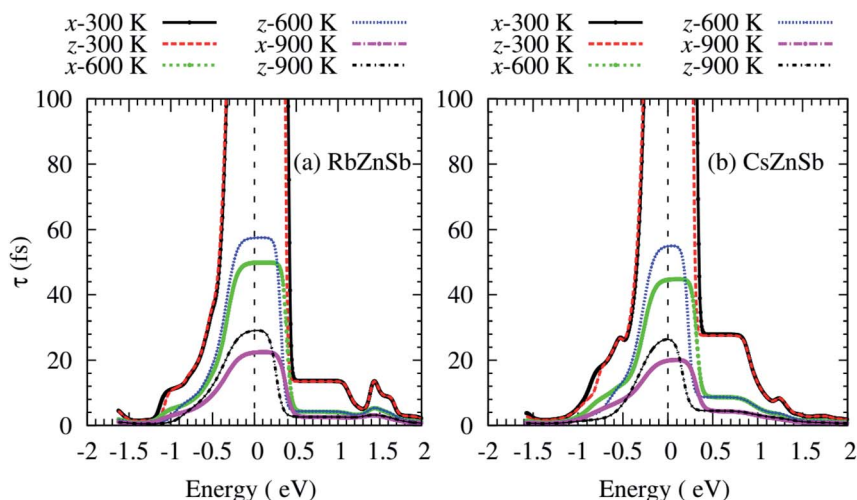


Fig. 6 Anisotropic carrier lifetime as a function of the energy of (a) RbZnSb, and (b) CsZnSb at three consecutive temperatures. The dashed vertical lines at zero energy represent the Fermi level.

where Ω and \hbar are the unit cell volume and reduced Planck's constant. Also, ν stands for the index of phonon modes, $\bar{\omega}_\nu$ for the averaged frequency of phonon modes, g_ν^2 for the averaged of the electron-phonon matrix, $n(\bar{\omega}_\nu, T)$ for the Bose-Einstein distribution function, $f(\varepsilon + \bar{\omega}_\nu, \mu, T)$ for the Fermi-Dirac distribution function, $g_s = 2$ for the degeneracy of spin, ε the energy of carriers, and ρ for the electronic density of states (DOS) per unit volume and energy.³⁴ Readers should consult with ref. 34 for further details.

The computed carrier lifetime of both compounds exhibits a strong energy dependency as shown in Fig. 6. The τ of AZnSb shows a weak anisotropic behavior at all temperatures. The variations of τ with energy can be explained by using the equation:³⁴

$$\tau^{-1} \sim g^2(\varepsilon)\rho(\varepsilon). \quad (2)$$

From the above equation, the carrier lifetime changes inversely with the electronic density of states (ρ) per-unit energy and per-unit volume of the unit cell. In this case, the g exhibits a weak energy dependency. The temperature similarly affects the τ .

Both compounds possess almost isotropic Seebeck coefficient (S) for n-type carriers and weakly anisotropic S for p-type carriers, and the S falls sharply with carrier concentrations, as shown in Fig. 7.

The S of these compounds are large and n-type carriers induce much larger S due to highly non-parabolic bands than

that of p-type carriers at certain carrier concentrations. At $2.49 \times 10^{20} \text{ cm}^{-3}$ carrier concentrations, the average S of n-type RbZnSb can reach up to $232.36 \mu\text{V K}^{-1}$ at 900 K while the S of p-type RbZnSb remains slightly higher, $237.97 \mu\text{V K}^{-1}$ at 900 K and $0.147 \times 10^{20} \text{ cm}^{-3}$. However, at $0.793 \times 10^{20} \text{ cm}^{-3}$ carrier concentrations, the S of n-type CsZnSb can reach up to $220 \mu\text{V K}^{-1}$ at 900 K while the S of p-type CsZnSb remains larger, $235.16 \mu\text{V K}^{-1}$ at 900 K and $0.149 \times 10^{20} \text{ cm}^{-3}$. Highly non-parabolic conduction band minima of n-type RbZnSb compared to that of n-type CsZnSb are responsible for larger Seebeck coefficient of n-type RbZnSb. On the other side, similar non-parabolic valence band maxima and effective mass of holes of p-type RbZnSb compared to that of p-type CsZnSb are responsible for identical Seebeck coefficient of both compounds for p-type carriers.

Electrical conductivity (σ) of AZnSb exhibits opposite trends compared to the Seebeck coefficient, *i.e.*, it sharply rises with carrier concentrations and decreases with temperature, as shown in Fig. 8. The σ of these compounds is also highly anisotropic like lattice thermal conductivity. As the alkali metal has negligible contributions to the electronic structure, the values of σ show a weak dependency on the alkali metal Rb/Cs.

Interestingly, the anisotropic nature of the σ for n-type carriers strongly depends on the alkali metal. The σ of n-type RbZnSb exhibits anisotropic behavior while the values σ of n-type CsZnSb are almost isotropic. Although the values of in-plane electrical conductivity of both compounds are high for p-type carriers due to lighter effective mass, the cross-plane σ

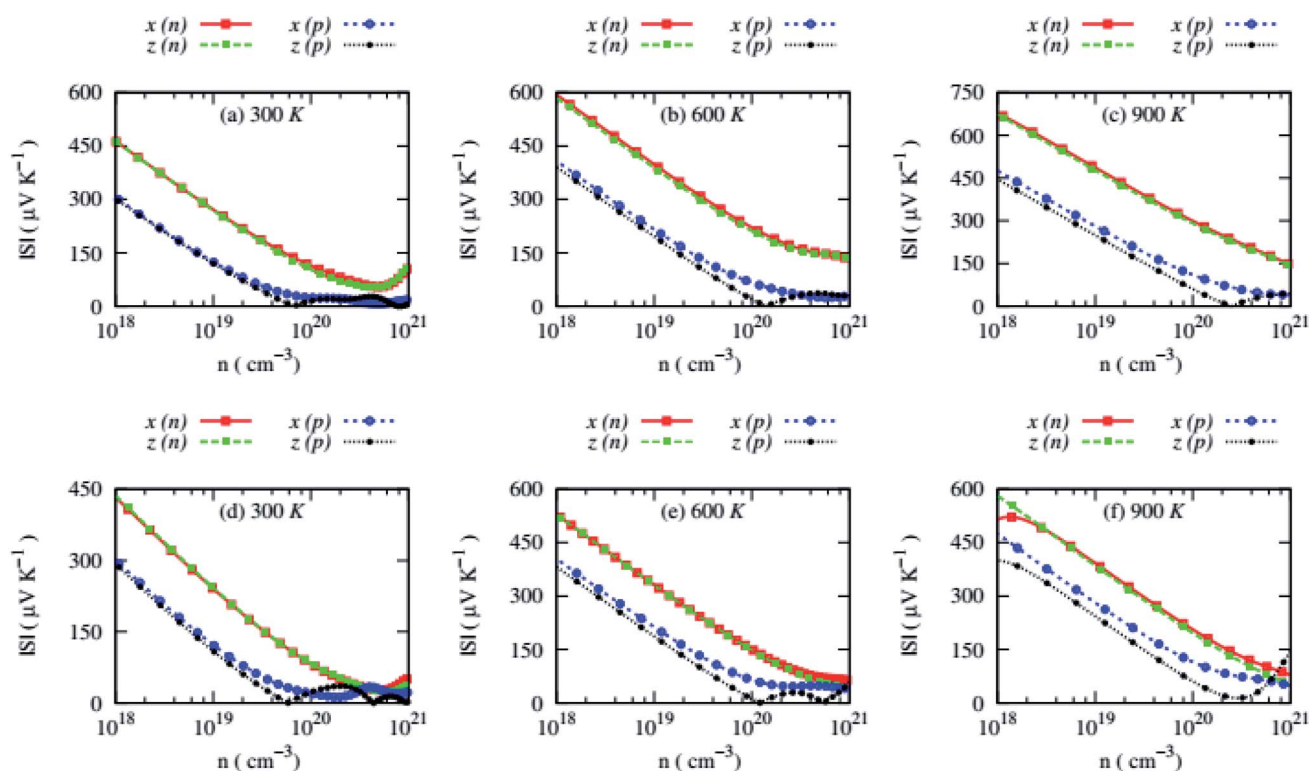


Fig. 7 Calculated absolute values of the anisotropic Seebeck coefficient ($|S|$) as a function of carrier concentrations of (a–c) RbZnSb and (d–f) CsZnSb for both n- and p-type carriers at three consecutive temperatures.

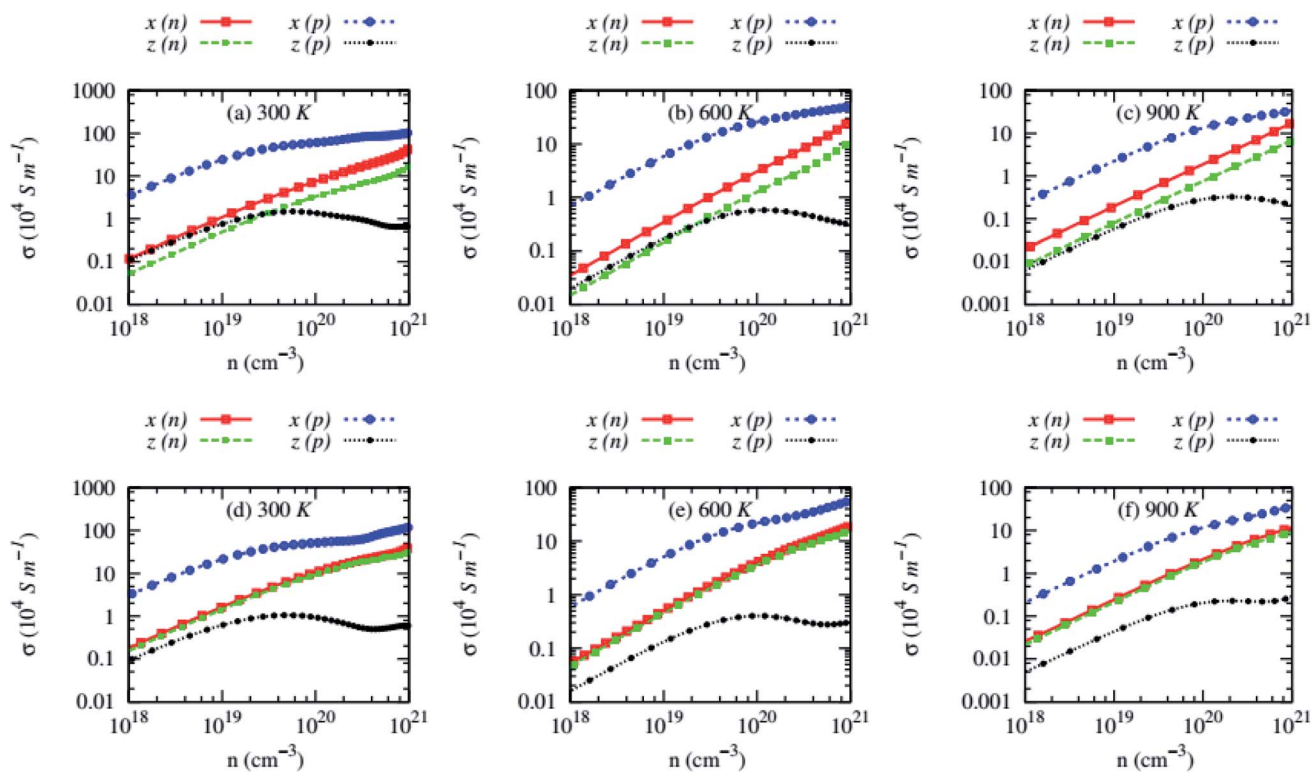


Fig. 8 Anisotropic electrical conductivity (σ) as a function of carrier concentrations of (a–c) RbZnSb and (d–f) CsZnSb for both n- and p-type carriers at three consecutive temperatures.

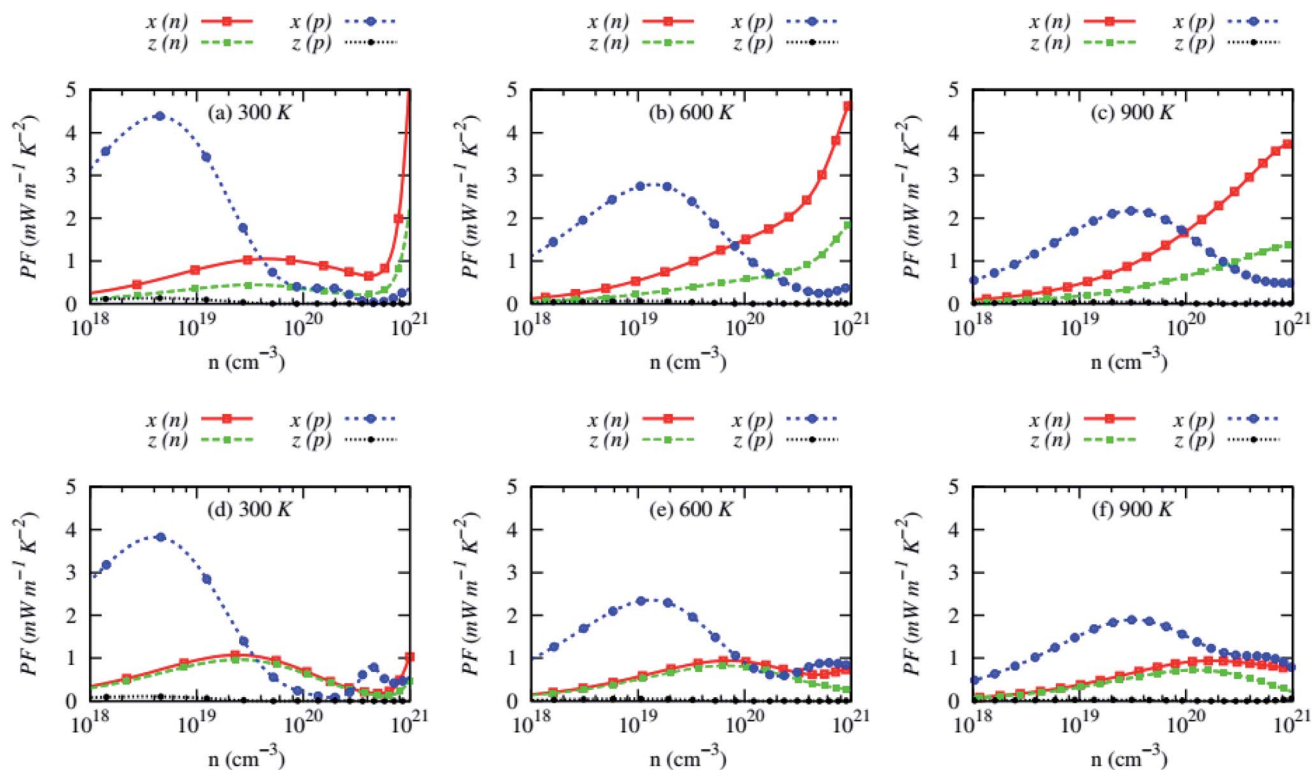


Fig. 9 Anisotropic power factor (PF) as a function of carrier concentrations of (a–c) RbZnSb and (d–f) CsZnSb for both n- and p-type carriers at three consecutive temperatures.

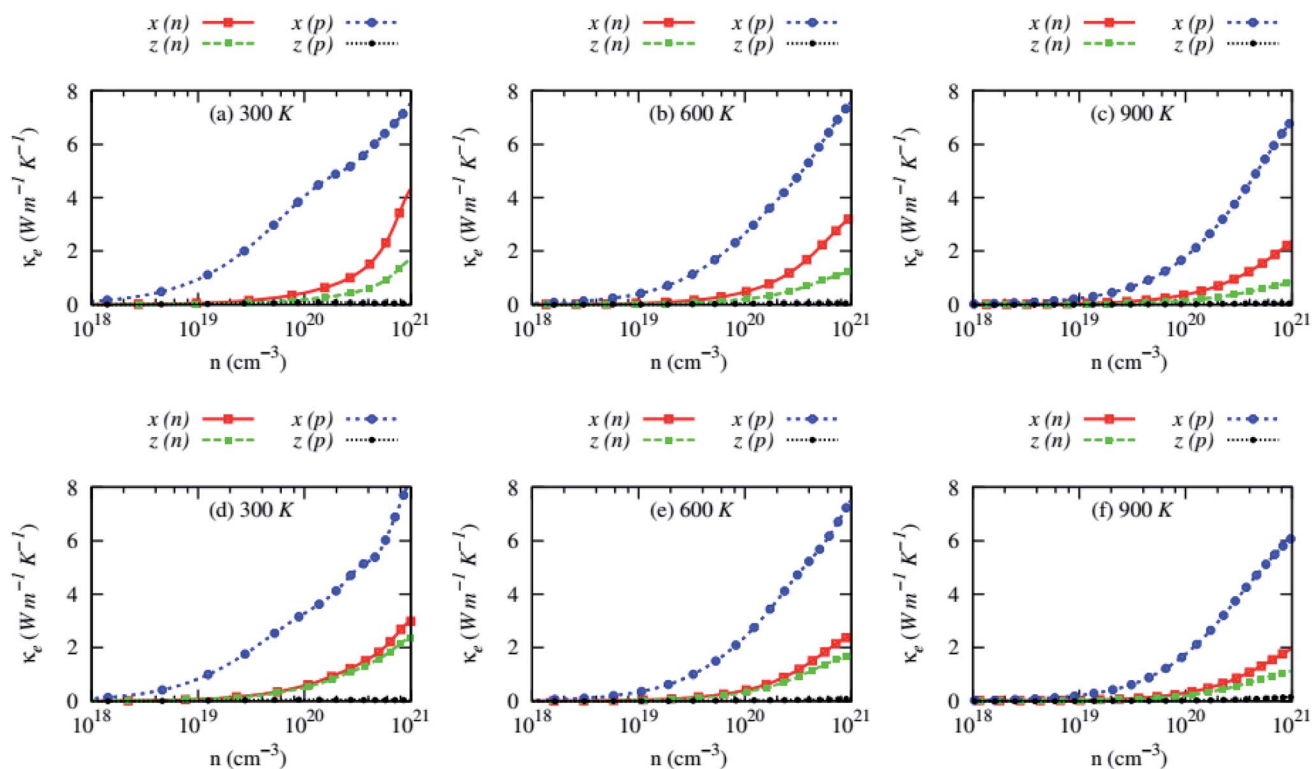


Fig. 10 Anisotropic electronic thermal conductivity (κ_e) as a function of carrier concentrations of (a–c) RbZnSb and (d–f) CsZnSb for both n- and p-type carriers at three consecutive temperatures.

values are exceptionally low at all temperatures, especially above 10^{20} cm^{-3} carrier concentrations. The cross-plane σ of p-type AZnSb decreases slightly above 10^{20} cm^{-3} . The carriers scattering above 10^{20} cm^{-3} might unprecedentedly rise along the z-direction.

The presence of multiple converged bands leads to forming the resonant level, which can be seen from the well-defined peak around the Fermi level in the electronic density of states, as shown in Fig. 5(b) and (d) for RbZnSb and CsZnSb, respectively. These bands are responsible for the abnormal rise/fall for Seebeck coefficient and electrical conductivity at high carrier concentrations above 10^{20} cm^{-3} . As the peak of conduction bands of CsZnSb is week-defined (please see Fig. 5(d)), the abnormal changes of Seebeck coefficient and electrical conductivity of n-type carriers above 10^{20} cm^{-3} are slower compared to that of other cases.

The electrical conductivity of both compounds, except cross-plane σ of p-type carriers, is relatively high despite their wide bandgap ~ 1.37 and 1.1 eV for RbZnSb and CsZnSb, respectively, which originates from the highly dispersive and degenerate bands, and relatively lighter effective mass. Notably, the electrical conductivity of RbZnSb is higher than that of CsZnSb, although its bandgap is comparatively wider, because of its lighter effective mass. The σ of AZnSb decreases with temperatures in all cases, suggesting the extrinsic nature of AZnSb compounds.

The carrier concentrations dependency of anisotropic power factor (PF) of AZnSb at three consecutive temperatures is shown in Fig. 9. Large Seebeck coefficient and high electrical conductivity along with in-plane lead to a high PF, reaching ~ 4 mW

$\text{m}^{-1} \text{K}^{-2}$ at 300 K. The PF of n-type RbZnSb is exceptionally high at high temperatures due to larger Seebeck coefficient while it remains low (~ 1 mW $\text{m}^{-1} \text{K}^{-2}$) for n-type CsZnSb at all studied temperatures. However, the cross-plane PF of p-type AZnSb is very small due to low electrical conductivity.

Fig. 10 demonstrates the carrier concentration dependency of the electronic part of the thermal conductivity. The electronic part of the thermal conductivity (κ_e) of both compounds is highly anisotropic and rises with carrier concentrations. The κ_e exhibits a weak dependency on the temperature. Like electrical conductivity, it decreases with the temperature slowly.

The in-plane κ_e values of p-type AZnSb is much higher than that of other carriers and plane. The cross-plane κ_e of p-type AZnSb is very low due to the unprecedented slowing of the mobility of the carrier along that axes.

In all cases (except cross-plane κ_e of p-type carriers), the electronic part of the thermal conductivity dominates over the

Table 3 Computed isotropic absolute value of Seebeck coefficient ($|S|$ ($\mu\text{V K}^{-1}$)), electrical conductivity (σ (10^4 S m^{-1})), power factor (PF (mW $\text{m}^{-1} \text{K}^{-2}$)), total thermal conductivity (κ_{tot} ($\text{W m}^{-1} \text{K}^{-1}$)), thermoelectric figure of merit (ZT) at carrier concentration n (10^{19} cm^{-3}) of AZnSb at a fixed carrier concentration

Compound	n	$ S $	σ	PF	κ_{tot}	ZT
RbZnSb	n	24.95	232.36	3.614	1.95	1.44
	p	1.471	237.97	2.146	1.21	0.99
CsZnSb	n	7.936	220.01	1.670	0.81	0.84
	p	1.495	235.16	1.881	1.04	0.82

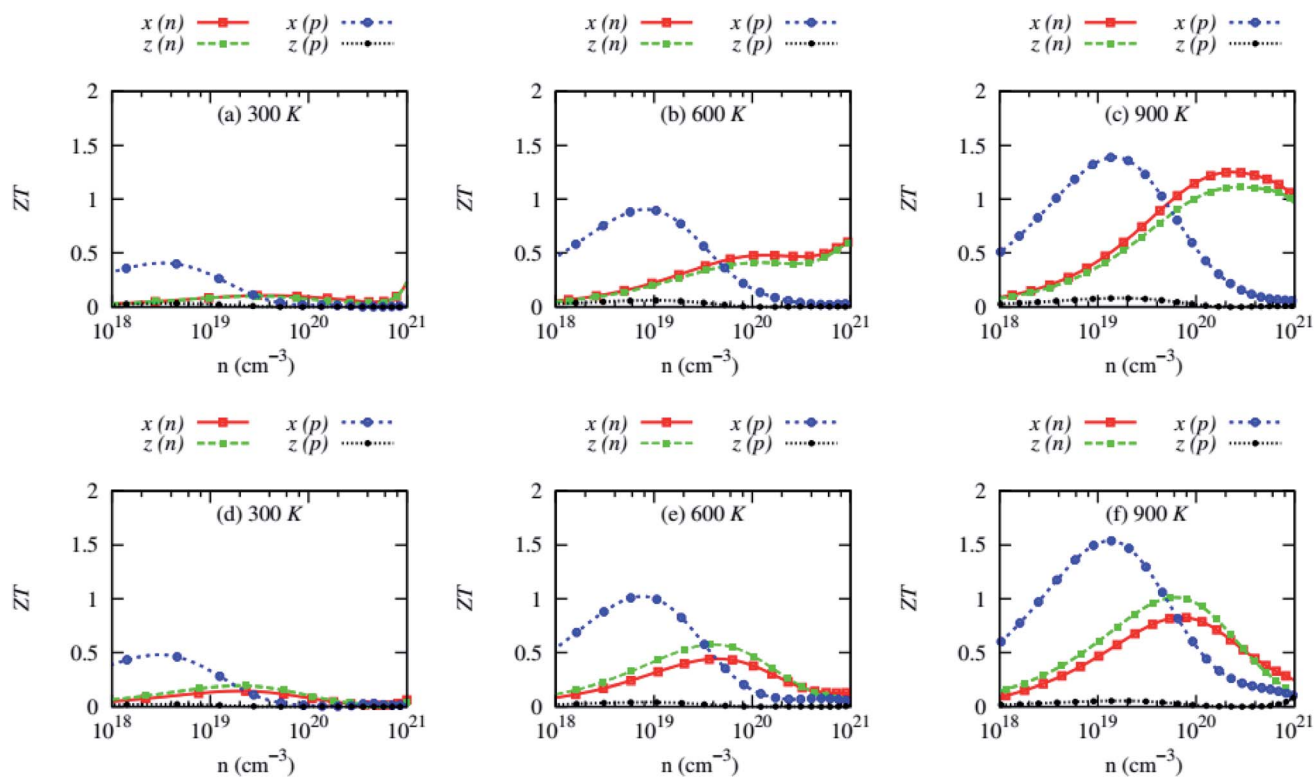


Fig. 11 Anisotropic thermoelectric figure of merit (ZT) as a function of carrier concentrations of (a–c) RbZnSb and (d–f) CsZnSb for both n- and p-type carriers at three consecutive temperatures.

lattice thermal conductivity at high temperatures (from 600 K in Fig. 10). The computed transport coefficients of these compounds at optimum carrier concentrations and 900 K for both types of carriers are listed in Table 3.

3.4. Thermoelectric performance

The large PF, low electronic part of the thermal conductivity, and lattice thermal conductivity lead to a high thermoelectric figure of merit (ZT), as shown in Fig. 11. The values of ZT of both

compounds are anisotropic and strongly depend on the carrier crystallographic plane, especially for p-type carriers.

The room temperature ZT of both compounds is very small, suggesting that they are not suitable for low-temperature thermoelectric applications, despite the in-plane ZT of p-type AZnSb can approach ~ 0.5 at 300 K and $\sim 5 \times 10^{18} \text{ cm}^{-3}$. The variation of the carrier concentrations has been obtained from the rigid shift of the Fermi level to describe the thermoelectric properties of the studied compounds. During the experimental synthesis,

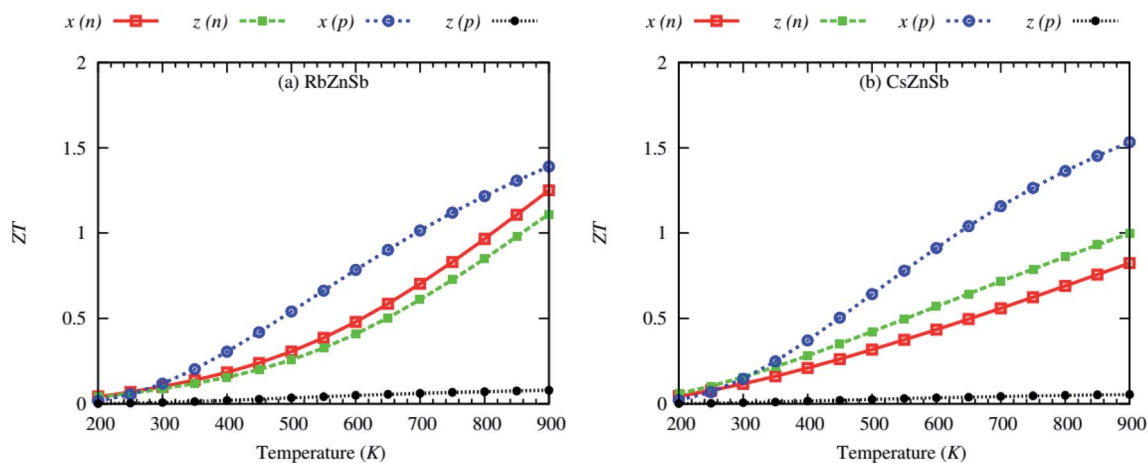


Fig. 12 Anisotropic thermoelectric figure of merit (ZT) as a function of the temperature of (a) RbZnSb and (b) CsZnSb for both n- and p-type carriers at fixed carrier concentrations.

the carrier concentration might be different or reached this optimum carrier concentration. But the calculated ZT at the optimum carrier concentrations, within the computational uncertainty, is expected to be obtainable experimentally. However, this does not necessarily describe the whole range of carrier concentrations of these compounds.

Although the in-plane ZT of p-type AZnSb is high, reaching ~ 1.5 at 900 K and $\sim 10^{19} \text{ cm}^{-3}$, the values of cross-plane ZT of both compounds for p-type carriers are impractically small due to low electrical conductivity. On the other side, the ZT of n-type AZnSb is less anisotropic and the value of RbZnSb and CsZnSb can reach a maximum of 1.22 and 0.87 at 900 K and $\sim 10^{20} \text{ cm}^{-3}$, respectively.

Fig. 12 demonstrates the effect of temperature on the thermoelectric performance of AZnSb at fixed carrier concentrations $\sim 10^{20} \text{ cm}^{-3}$ and $\sim 10^{19} \text{ cm}^{-3}$ for n- and p-type carriers, respectively (for temperature-dependent transport coefficients, please see ESI†). The ZT sharply rises with temperature. This suggests that the ZT would be higher above 900 K. However, the experimental melting or decomposition temperature of RbZnSb and CsZnSb is 975 and 1040 K, respectively. Thus, the ZT above 900 K has not been studied.

Table 3 lists the calculated isotropic (average $ZT = \frac{1}{3}(ZT_x + ZT_y + ZT_z)$) of AZnSb at 900 K and fixed carrier concentration. On average, the ZT of RbZnSb is 1.22 and 1.1 at 900 K for p- and n-type carriers, respectively. On the other side, the average ZT of CsZnSb is slightly smaller but it is 0.87 and 1.14 at 900 K for p- and n-type carriers, respectively, within the computational accuracy. Therefore, the high values of the thermoelectric figure of merit (ZT) of layered AZnSb compounds suggest that they are potential materials for thermoelectric device applications, and experimental studies are encouraged to confirm this prediction.

4. Conclusions

In summary, systematic first-principles calculations have been performed to study structural, phonon transport, electronic structure, and carrier transport properties of AZnSb (A = Rb, Cs). Layered AZnSb compounds have low Debye temperature. The presence of heavier elements Rb/Cs causes phonon softening and leads to larger values of the mode Grüneisen parameter, expanding over negative and positive values, *i.e.*, high anharmonicity. This leads to intense phonon scattering in both compounds and hence, low lattice thermal conductivity (κ_l), ($\sim 0.5 \text{ W m}^{-1} \text{ K}^{-1}$ on the average at 900 K). Both compounds are direct bandgap (~ 1.37 and 1.1 eV for RbZnSb and CsZnSb, respectively) semiconductors, and Zn-3d and Sb-5p states mainly formulate the bandgap, with negligible contributions from alkali metal Rb/Cs. The electronic bands are highly dispersive and two-fold degenerate. The CBM and VBM are also highly non-parabolic. The non-parabolic bands and wider bandgap of AZnSb induce a large Seebeck coefficient. The dispersive and two-fold degenerate characters of bands are responsible for the relatively high electrical conductivity of AZnSb. In a combination of larger Seebeck coefficient and

electrical conductivity, both compounds have a larger power factor. The large power factor and low values of κ_l lead to a high average thermoelectric figure of merit (ZT) of RbZnSb and CsZnSb, reaching 1.22 and 1.1 and 0.87 and 1.14 at 900 K for p- and n-type carriers, respectively. Therefore, AZnSb are potential materials for high-temperature thermoelectric device applications.

Data availability statement

The data that support the findings of this study are available from the corresponding author upon reasonable request.

Conflicts of interest

There are no conflicts to declare.

References

- 1 L. M. Schoop, F. Pielnhofer and B. V. Lotsch, *Chem. Mater.*, 2018, **30**, 3155–3176.
- 2 B. Owens-Baird, L.-L. Wang, S. Lee and K. Kovnir, *Z. Anorg. Allg. Chem.*, 2020, **646**, 1079–1085.
- 3 Q. Xu, Z. Song, S. Nie, H. Weng, Z. Fang and X. Dai, *Phys. Rev. B: Condens. Matter Mater. Phys.*, 2015, **92**, 205310.
- 4 B. R. Bennett, R. Magno, J. B. Boos, W. Kruppa and M. G. Ancona, *Solid-State Electron.*, 2005, **49**, 1875–1895.
- 5 H. Kleinke, *Chem. Mater.*, 2010, **22**, 604–611.
- 6 G. Li and C. Felser, *Appl. Phys. Lett.*, 2020, **116**, 70501.
- 7 J. Sotor, G. Sobon, K. Grodecki and K. M. Abramski, *Appl. Phys. Lett.*, 2014, **104**, 251112.
- 8 O. A. Tretiakov, A. Abanov, S. Murakami and J. Sinova, *Appl. Phys. Lett.*, 2010, **97**, 73108.
- 9 D. Takane, S. Souma, T. Sato, T. Takahashi, K. Segawa and Y. Ando, *Appl. Phys. Lett.*, 2016, **109**, 91601.
- 10 H. Kleinke, *Chem. Soc. Rev.*, 2000, **29**, 411–418.
- 11 V. Gvozdet'skiy, B. Owens-Baird, S. Hong, T. Cox, G. Bhaskar, C. Harmer, Y. Sun, F. Zhang, C.-Z. Wang, K.-M. Ho, *et al.*, *Chem. Mater.*, 2019, **31**, 8695–8707.
- 12 J. Wang and K. Kovnir, *J. Am. Chem. Soc.*, 2015, **137**, 12474–12477.
- 13 A. H. Sommer, *Appl. Phys. Lett.*, 1963, **3**, 62–63.
- 14 A. S. Mikhaylushkin, J. Nylén and U. Häussermann, *Chem.–Eur. J.*, 2005, **11**, 4912–4920.
- 15 E. K. Huang, D. Hoffman, B.-M. Nguyen, P.-Y. Delaunay and M. Razeghi, *Appl. Phys. Lett.*, 2009, **94**, 53506.
- 16 S. R. Brown, S. M. Kauzlarich, F. Gascoin and G. J. Snyder, *Chem. Mater.*, 2006, **18**, 1873–1877.
- 17 Y. Hu, G. Cerretti, E. L. K. Wille, S. K. Bux and S. M. Kauzlarich, *J. Solid State Chem.*, 2019, **271**, 88–102.
- 18 C. Yu, T.-J. Zhu, R.-Z. Shi, Y. Zhang, X.-B. Zhao and J. He, *Acta Mater.*, 2009, **57**, 2757–2764.
- 19 S. Chen and Z. Ren, *Mater. Today*, 2013, **16**, 387–395.
- 20 H. J. Goldsmid, *Introduction to thermoelectricity*, Springer, 2010, vol. 121.
- 21 H. J. Goldsmid, *Thermoelectric refrigeration*, Springer, 2013.

- 22 A. Ioffe, *Semiconductor Thermoelements and Thermoelectric Cooling*, Infosearch, London, 1st edn, 1957.
- 23 S. Chandra and K. Biswas, *J. Am. Chem. Soc.*, 2019, **141**(15), 6141–6145.
- 24 C. J. Vineis, A. Shakouri, A. Majumdar and M. G. Kanatzidis, *Adv. Mater.*, 2010, **22**, 3970–3980.
- 25 S. D. Kang, J.-H. Pöhls, U. Aydemir, P. Qiu, C. C. Stoumpos, R. Hanus, M. A. White, X. Shi, L. Chen, M. G. Kanatzidis, *et al.*, *Materials Today Physics*, 2017, **1**, 7–13.
- 26 M. Wambach, R. Stern, S. Bhattacharya, P. Ziolkowski, E. Müller, G. K. H. Madsen and A. Ludwig, *Adv. Electron. Mater.*, 2016, **2**, 1500208.
- 27 X. Zhang, L. Yu, A. Zakutayev and A. Zunger, *Adv. Funct. Mater.*, 2012, **22**, 1425–1435.
- 28 D. Koller, F. Tran and P. Blaha, *Phys. Rev. B: Condens. Matter Mater. Phys.*, 2011, **83**, 195134.
- 29 P. Gorai, A. Ganose, A. Faghaninia, A. Jain and V. Stevanović, *Mater. Horiz.*, 2020, **7**, 1809–1818.
- 30 P. Giannozzi, S. Baroni, N. Bonini, M. Calandra, R. Car, C. Cavazzoni, D. Ceresoli, G. L. Chiarotti, M. Cococcioni, I. Dabo, *et al.*, *J. Phys.: Condens. Matter*, 2009, **21**, 395502.
- 31 J. P. Perdew, A. Ruzsinszky, G. I. Csonka, O. A. Vydrov, G. E. Scuseria, L. A. Constantin, X. Zhou and K. Burke, *Phys. Rev. Lett.*, 2008, **100**, 136406.
- 32 J. P. Perdew, K. Burke and M. Ernzerhof, *Phys. Rev. Lett.*, 1996, **77**, 3865.
- 33 A. Dal Corso, *Comput. Mater. Sci.*, 2014, **95**, 337–350.
- 34 G. Samsonidze and B. Kozinsky, *Adv. Energy Mater.*, 2018, **8**, 1800246.
- 35 S. Bang, J. Kim, D. Wee, G. Samsonidze and B. Kozinsky, *Materials Today Physics*, 2018, **6**, 22–30.
- 36 G. K. H. Madsen and D. J. Singh, *Comput. Phys. Commun.*, 2006, **175**, 67–71.
- 37 P. Blaha, K. Schwarz, F. Tran, R. Laskowski, G. K. H. Madsen and L. D. Marks, *J. Chem. Phys.*, 2020, **152**, 74101.
- 38 P. Blaha, K. Schwarz, G. K. H. Madsen, D. Kvasnicka, J. Luitz, R. Laskowski, F. Tran L. D. Marks and WIEN2k, *Augmented Plane Wave + Local Orbitals Program for Calculating Crystal Properties*, ed. K. Schwarz, Techn. Universität Wien, Austria, 2018, ISBN 3-9501031-1-2.
- 39 A. Togo, L. Chaput and I. Tanaka, *Phys. Rev. B: Condens. Matter Mater. Phys.*, 2015, **91**, 94306.
- 40 A. Seko, A. Togo, H. Hayashi, K. Tsuda, L. Chaput and I. Tanaka, *Phys. Rev. Lett.*, 2015, **115**, 205901.
- 41 K. Mizokami, A. Togo and I. Tanaka, *Phys. Rev. B*, 2018, **97**, 224306.
- 42 H. Uchiyama, Y. Oshima, R. Patterson, S. Iwamoto, J. Shiomi and K. Shimamura, *Phys. Rev. Lett.*, 2018, **120**, 235901.
- 43 O. L. Anderson, *J. Phys. Chem. Solids*, 1963, **24**, 909–917.
- 44 F. Mouhat and F.-X. Coudert, *Phys. Rev. B: Condens. Matter Mater. Phys.*, 2014, **90**, 224104.
- 45 H. B. Ozisik, E. Deligoz, H. Ozisik and E. Ateser, *Mater. Res. Express*, 2020, **7**, 25004.
- 46 J. Shiomi, K. Esfarjani and G. Chen, *Phys. Rev. B: Condens. Matter Mater. Phys.*, 2011, **84**, 104302.
- 47 M. T. Dove, V. Heine and K. D. Hammonds, *Mineral. Mag.*, 1995, **59**, 629–639.
- 48 S. Mukhopadhyay, D. S. Parker, B. C. Sales, A. A. Puretzky, M. A. McGuire and L. Lindsay, *Science*, 2018, **360**, 1455–1458.
- 49 M. Sajjad, N. Singh, S. Sattar, S. De Wolf and U. Schwingenschlögl, *ACS Appl. Energy Mater.*, 2019, **2**, 3004–3008.
- 50 L.-D. Zhao, S.-H. Lo, Y. Zhang, H. Sun, G. Tan, C. Uher, C. Wolverton, V. P. Dravid and M. G. Kanatzidis, *Nature*, 2014, **508**, 373.
- 51 M. Sajjad, Q. Mahmood, N. Singh and J. A. Larsson, *ACS Appl. Energy Mater.*, 2020, **3**(11), 11293–11299.
- 52 L. Huang, R. He, S. Chen, H. Zhang, K. Dahal, H. Zhou, H. Wang, Q. Zhang and Z. Ren, *Mater. Res. Bull.*, 2015, **70**, 773–778.
- 53 T. Sekimoto, K. Kurosaki, H. Muta and S. Yamanaka, *Mater. Trans.*, 2006, **47**, 1445–1448.
- 54 Y. Xia, S. Bhattacharya, V. Ponnambalam, A. L. Pope, S. J. Poon and T. M. Tritt, *J. Appl. Phys.*, 2000, **88**, 1952–1955.